Journal of Physics and Chemistry of Solids 202 (2025) 112649

Contents lists available at ScienceDirect

Journal of Physics and Chemistry of Solids

journal homepage: www.elsevier.com/locate/jpcs

Co-doped $FeNbO_4$: Simple synthesis, DFT calculations and electrocatalytic performance for the hydrogen evolution reaction in alkaline medium

Raí F. Jucá [a,i], Diego S. Evaristo [b], Francisco G.S. Oliveira [b,*], Luís P.M. Santos [c], Gilberto D. Saraiva [b], Antonio J.R. Castro [d], Nilson S. Ferreira [a,i], Luiz F. Lobato [e], João M. Soares [f], Anna Luiza B. Brito [g], Rui Fausto [g,h], Marcelo A. Macêdo [a], Benilde F.O. Costa [i]

[a] Departamento de Física, Universidade Federal de Sergipe, São Cristóvão, 49100-000, Sergipe, Brazil
[b] Faculdade de Educação Ciências e Letras do Sertão Central, Universidade Estadual do Ceará, Quixadá, CE, 62902-098, Brazil
[c] Programa de Pós-Graduação em Engenharia e Ciência de Materiais, Centro de Tecnologia, Universidade Federal do Ceará, Campus do Pici, Bloco 729, 60440-900, Fortaleza, CE, Brazil
[d] Universidade Federal do Ceará, Campus Quixadá, Quixadá, CE, 63902-580, Brazil
[e] Institute of Criminalistics, Scientific Police of Pará, Marabá, PA, 68507-000, Brazil
[f] Departamento de Física, Universidade do Estado do Rio Grande do Norte, 59610-210, Mossoró, RN, Brazil
[g] University of Coimbra, CQC-IMS, Department of Chemistry, P-3004-535, Coimbra, Portugal
[h] Istanbul Kultur University, Spectroscopy@IKU, Faculty of Sciences and Letters, Department of Physics, Bakirkoy, Istanbul, 34158, Türkiye
[i] University of Coimbra, CFisUC, Department of Physics, P-3004-516, Coimbra, Portugal

ARTICLE INFO

Keywords:
$FeNbO_4$
DFT calculations
SEM
Cobalt-doped and hydrogen evolution reaction

ABSTRACT

Cobalt-doped iron niobate samples, $Fe_{(1-x)}Co_xNbO_4$ ($0 \leq x \leq 0.20$), synthesized by the solid-state reaction method, were characterized using X-ray diffraction (XRD), Raman spectroscopy, scanning electron microscopy (SEM) and energy dispersive spectroscopy (EDS). Density functional theory (DFT) calculations was employed to assign the experimental Raman modes of $FeNbO_4$ and for cobalt-doped iron niobate, as the Raman spectra showed no significant changes in the profile upon doping. The crystal structure was successfully refined in the monoclinic system with the P21/n space-group symmetry, containing two formula units per unit cell ($Z = 2$). SEM analysis revealed particles with irregular morphology, and the average crystallite size increased with cobalt doping ($\langle D \rangle = 28.0 \pm 1.6$ μm). EDS confirmed the incorporation of cobalt into the samples. Electrochemical measurements demonstrated promising hydrogen evolution reaction (HER) activity, with an overpotential of approximately 620 mV at a current density of 10 mA/cm^2 and a Tafel slope of 156 mV/dec for the $Fe_{0.80}Co_{0.20}NbO_4$ composition. Additionally, a negligible loss of overpotential was observed after 10 consecutive hours of hydrogen evolution. These findings indicate that incorporating Co^{2+} ions into the iron niobate ($FeNbO_4$) matrix significantly enhances the material's electrocatalytic performance. The promising results suggest that Co-doped $FeNbO_4$, as a noble metal-free electrocatalyst, holds considerable potential for applications in sustainable hydrogen production.

1. Introduction

The rapid advancement of modern society and the global economy has increased the demand for innovative and clean energy solutions. In parallel, the depletion of conventional fossil fuel reserves, exploration of sustainable energy sources, and growing concerns over environmental pollution, particularly greenhouse gas emissions, have emerged as global priorities [1–3]. Hydrogen has been identified as a promising alternative due to its high energy density, renewability, and clean byproducts [4]. Molecular hydrogen (H_2) can be produced through various methods, with water electrolysis standing out for its efficiency. This process involves two primary reactions: the hydrogen evolution reaction (HER) at the cathode and the oxygen evolution reaction (OER) at the anode, making it a promising approach for large-scale hydrogen

* Corresponding author.
E-mail address: francisco.gilvane@uece.br (F.G.S. Oliveira).

https://doi.org/10.1016/j.jpcs.2025.112649
Received 8 January 2025; Received in revised form 10 February 2025; Accepted 23 February 2025
Available online 28 February 2025

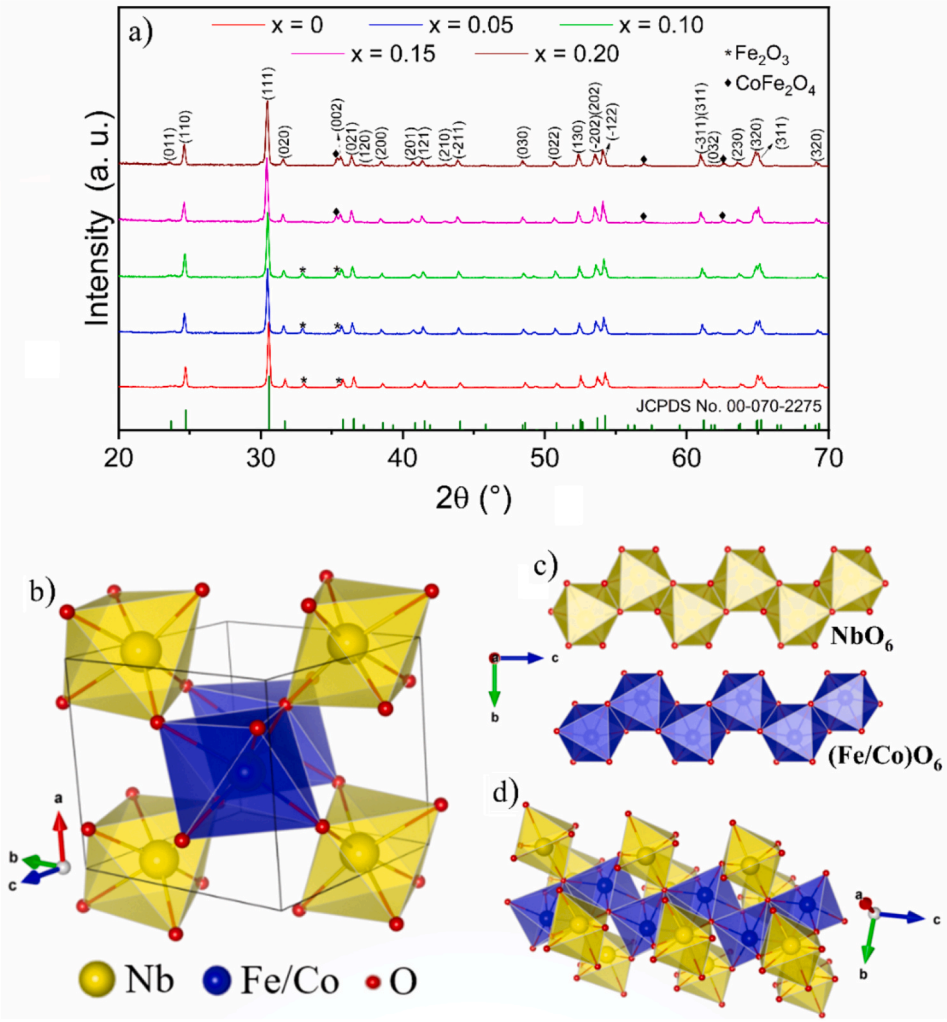

Fig. 1. (a) X-ray diffraction patterns of the $Fe_{(1-x)}Co_xNbO_4$ ($0.0 \leq x \leq 0.20$) samples. (b) Unit cell of the $Fe_{(1-x)}Co_xNbO_4$ in the monoclinic symmetry structure with $P2_1/c$ (C_{2h}^{13}) space group. (c) Zigzag chains of (Fe/Co)O_6 and NbO_6 octahedra, sharing edges parallel to the c axis. (d) Zigzag chains intersect of (Fe/Co)O_6 and NbO_6 octahedra, sharing edges parallel to the long c axis.

production [5]. Currently, the state-of-art of electrocatalyst materials used to promote both reactions are based on noble metal, such as platinum (Pt), palladium (Pd), and ruthenium (Ru). However, the high cost and limited availability of noble metal-based catalysts present substantial barriers. Consequently, developing HER catalysts that utilize non-noble metals, while achieving high catalytic activity and durability, remains a critical challenge. This need has driven researchers to investigate the potential of other materials, especially transition metals, which are more cost-effective and abundant in the Earth's crust in the form of ores [6–8].Transition metal oxides, carbides, sulfides, and nitrides have been extensively studied for their HER activity [8–11]. However, achieving high stability for catalysts in both alkaline and acidic environments remains challenging, often limiting their durability in water electrolysis applications [12]. The bimetallic oxide $FeNbO_4$, known for its robustness under extreme conditions, shows considerable promise for providing enhanced stability in the water electrolysis process. Iron-based materials (Fe) are favored for their high catalytic activity, affordability, and natural abundance [13]. Niobium (Nb), on the other hand, contributes excellent electrochemical and catalytic properties [14,15], making it a promising candidate for further HER studies. $FeNbO_4$ has also been widely studied in other domains for its magnetic [16–18], dielectric [19,20], morphological [20], structural, and vibrational properties [16,21]. Despite these investigations, there remains a need for more detailed analysis on its vibrational properties. Additionally, there is a growing interest in theoretical studies involving density functional theory (DFT) to explore its properties further [22,23].

Several strategies have been developed to enhance the physical and chemical properties of iron niobate ($FeNbO_4$) and its applications, including the *in-situ* growth of ferric niobate in porous carbon [24] and the use of carbon dioxide in reductive reactions during synthesis [25]. Among these methods, the doping transition metals has demonstrated particularly effectiveness in optimizing the structure and improving its properties [16,26]. The role of redox-active cations is pivotal in doping, as they serve as intermediary agents, that facilitate the modulation of the electronic structure of $FeNbO_4$. These cations can interact directly with the active sites of the material, thereby adjusting the electronic density and promoting more efficient redox reactions. This modulation of electronic properties contributes to an improved electrochemical performance of the material [27–31]. Consequently, understanding the substitution at the lattice site by ions with varying ionic radii and mixed valence states can significantly enhance the properties of $FeNbO_4$.

In this context, the process of Co^{2+} ions doping in electrocatalysts has been widely explored as an effective strategy to enhance catalytic activity in HER. Studies have shown that the incorporation of Co^{2+} ions can reduce the adsorption energy of hydrogen on the catalyst surface and improve the reaction kinetics. For instance, Zhu et al. [32], using DFT calculations, demonstrated that Co doping in VSe_2 significantly reduces the Gibbs free energy for hydrogen adsorption (ΔG_H),

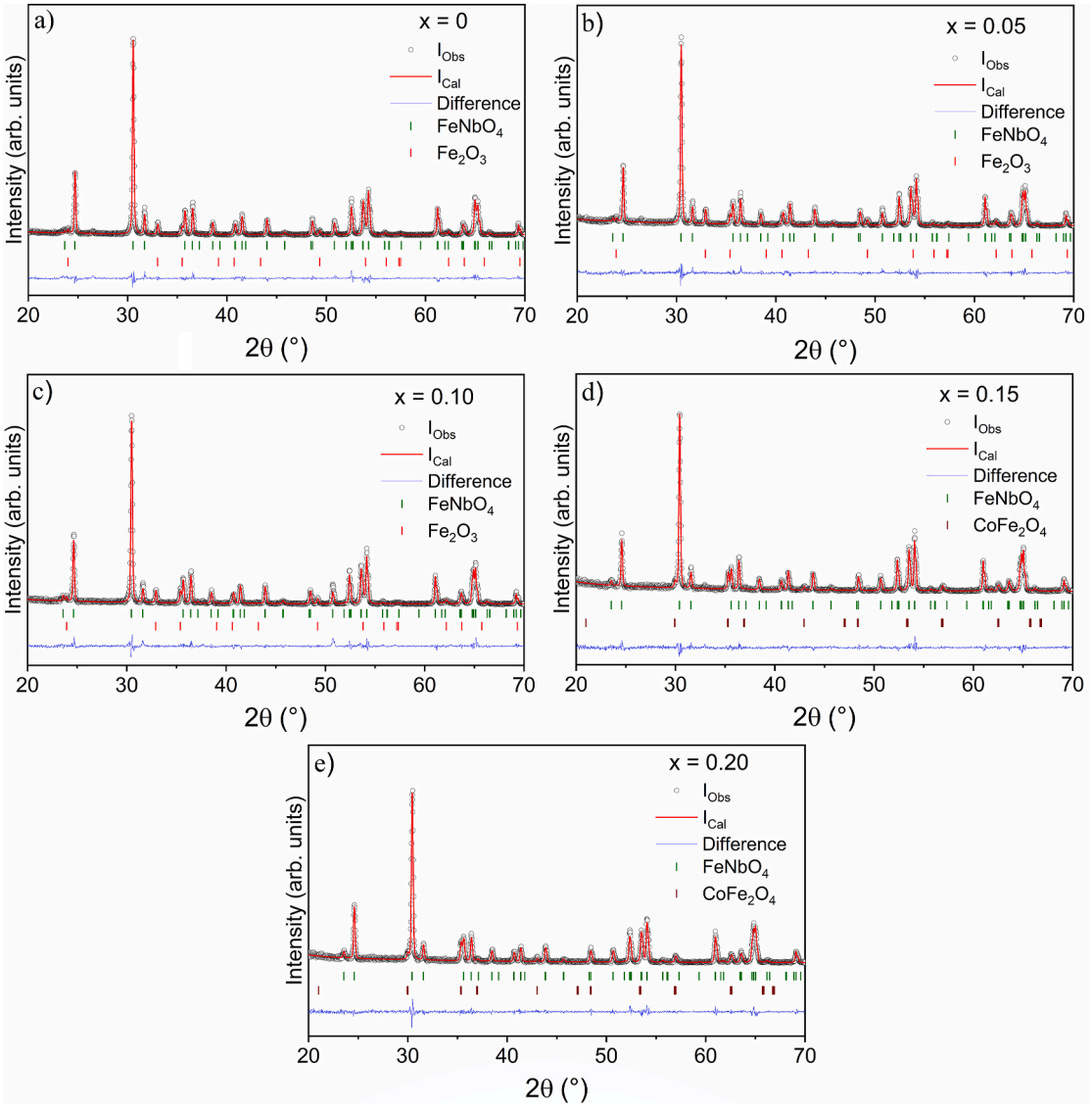

Fig. 2. Observed (gray), calculated (red), and differential (blue) patterns of Rietveld refinements of X-ray diffraction for $Fe_{(1-x)}Co_xNbO_4$ polycrystalline. (a) $x = 0.0$, (b) $x = 0.05$, (c) $x = 0.10$, (d) $x = 0.15$ and (e) $x = 0.20$. The gray circles symbols and the red line denote the observed and calculated intensities, respectively. Short verticals green, red and wine indicate the position of the possible Bragg reflections of the $FeNbO_4$, Fe_2O_3 and $CoFe_2O_4$ phase, respectively. The difference between the observed and calculated profiles blue is plotted at the bottom. (For interpretation of the references to colour in this figure legend, the reader is referred to the Web version of this article.)

promoting higher catalytic efficiency. Similarly, Lin et al. [33] found that introducing Co into Mo_2C nanowires substantially improved catalytic activity by reducing the overpotential and enhancing catalyst stability. Moreover, Dai et al. [34], showed that Co doping in MoS_2 generates an active CoMoS phase, optimizing hydrogen adsorption and improving HER kinetics. This study investigates the effects of substituting Fe^{3+} ions with Co^{2+} ions on the structural, vibrational, morphological, and, most notably, electrochemical properties of the $FeNbO_4$. Additionally, density functional theory (DFT) studies have been conducted to gain deeper insights into the vibrational properties. Furthermore, understanding the structural evolution under reaction can provide valuable insights into the effects of cobalt doping.

2. Experimental and theory section

2.1. Synthesis

Polycrystalline samples of iron-cobalt niobate, $Fe_{(1-x)}Co_xNbO_4$ ($0 \leq x \leq 0.20$), were synthesized using the solid-state reaction technique, which involves the homogenization of the powder precursor samples. Stoichiometric amounts of iron oxide (Fe_2O_3, Sigma-Aldrich, 99 %), niobium oxide (Nb_2O_5, Sigma-Aldrich, 99 %), and cobalt (II) sulfate ($CoSO_4.7H_2O$, Merk, 97 %) were used in the starting powder mixture. This mixture underwent heat treatment at 600 °C for 2 h in an ambient atmosphere. Following heat treatment, the mixture was subjected to a grinding process at a speed of 200 rpm for 20 min, after which it was sintered at 1200 °C for 24 h.

2.2. Electrochemical measurements

All electrochemical characterization studies were conducted using a potentiostat/galvanostat (AUTOLAB PGSTAT30, Metrohm-Eco Chemie), controlled by NOVA software version 2.11, in a standard three-electrode configuration within a 1 mol/L NaOH alkaline solution at 298 K. Initially, an ink was prepared by dispersing 10 mg of catalyst material in 950 μ L of ethanol and 50 μ L of a Nafion solution (10 wt%), followed by homogenization via ultrasonication for 30 min. The working electrode was then prepared by drop-casting 1 μ L of the ink onto a

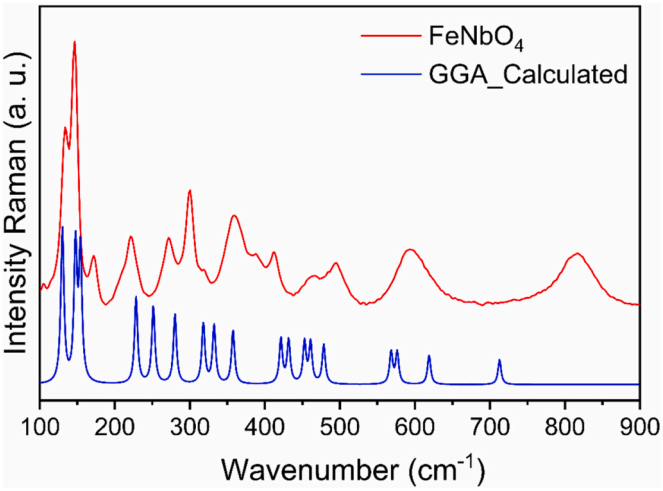

Fig. 3. Experimental and calculated Raman spectra of $FeNbO_4$ in the 100-900 cm^{-1} region.

Table 1
Observed and calculated Raman modes for the $FeNbO_4$, together with their assignments based on DFT calculations for the monoclinic phase.

Raman ω_{obs}	*Raman* ω_{cal}	*sym*	*Assignments modes*
133.72	*132.81*	B_g	$T_x[NbO_6]$
146.60	*150.69*	A_g	$T_y[NbO_6 + FeO_6]$
172.01	*157.69*	B_g	$T_{xz}[NbO_6 + FeO_6]$ in the diagonal of the xz plane
209.16	*233.02*	B_g	$T_{xyz}[NbO_6 + FeO_6]$
222.06	*256.45*	B_g	Lib $[NbO_6 + FeO_6]$
271.96	*285.88*	A_g	Bend $[NbO_6 + FeO_6]$ of strong motion of Fe atoms
299.83	*324.48*	A_g	Bend $[NbO_6 + FeO_6]$ of moderate motion of Fe atoms along y-axis
318.92	*339.11*	B_g	Bend $[NbO_6 + FeO_6]$
359.41	*364.90*	B_g	Lib $[NbO_6 + FeO_6]$
389.71	*429.91*	A_g	Bend $[NbO_6 + FeO_6]$
412.62	*440.50*	B_g	Bend $[NbO_6 + FeO_6]$
464.28	*462.05*	A_g	Bend $[NbO_6 + FeO_6]$ strong motion of O in the Fe–*O*–Nb bonds
494.61	*470.31*	B_g	Bend $[NbO_6 + FeO_6]$
	488.22	A_g	Bend $[NbO_6 + FeO_6]$
583.64	*579.82*	B_g	Asymmetric stretching $[FeO_6]$ + Bend $[NbO_6]$
599.26	*588.14*	A_g	Symmetric stretching $[NbO_6]$ + Bend $[FeO_6]$
622.30	*631.48*	B_g	Asymmetric stretching $[NbO_6]$ + Bend $[FeO_6]$
814.51	*727.29*	A_g	Symmetric stretching $[NbO_6]$ + Bend $[FeO_6]$

Bend: Bending, Lib: Libration, T: Translation.

glassy carbon electrode with a 3 mm diameter and subsequently allowed to dry at room temperature. The counter electrode used was a platinum plate, while a saturated $Ag_{(s)}/AgCl_{(s)}$ electrode (in KCl) served as the reference electrode. Linear scan voltammetry (LSV) was performed at a scan rate of 5 mV/s, with potential ranging from 0 to −850 mV (vs. the reversible hydrogen electrode, RHE). Electrochemical impedance spectroscopy (EIS) was conducted by applying a direct current potential of −290 mV (vs. RHE), with frequency ranges from 100 kHz to 50 mHz and an amplitude of 10 mV. Stability tests were performed using chronopotentiometry at a current density of 10 mA/cm^2 for a duration of 10 h. All potentials measured in this study were normalized to the reversible hydrogen electrode (RHE) using Equation (1).

$$E_{vs.RHE} = E_{vs.Ag/AgCl.KClsaturated} + 0.197 + 0.0591pH \quad (1)$$

2.3. Computational details

Vibrational properties of $FeNbO_4$ were computed using Density Functional Theory (DFT) as implemented in the Cambridge Serial Total Energy Package (CASTEP) [35]. This first-principles quantum mechanical software is developed for modeling materials and employs plane wave sets and pseudopotentials. Norm-conserving pseudopotential [36] were used to accurately account for electron exchange and correlation effects. The Generalized Gradient Approximation (GGA) with the Perdew-Burke-Ernzerhof (PBE) functional [37] was employed, utilizing a 3 × 3 × 3 Monkhorst-Pack grid [38]. A k-point was chosen with an energy cutoff of 900 eV and a specified energy tolerance per atom. Geometry optimization was performed using the Broyden–-Fletcher–Goldfarb–Shanno (BFGS) algorithm [39], with specific convergence criteria: a maximum energy change of 1.0×10^{-5} eV/atom, a maximum force of 0.03 eV/Å, a maximum stress of 0.1 GPa, and a displacement of 0.001 Å. The electronic wave function was propagated through the reciprocal lattice along the high-symmetry paths in the Brillouin Zone (BZ) of the monoclinic crystal, specifically following the points Z(0.000, 0.000, 5.000) – G(0.000, 0.000, 0.000) – Y(0.000, 0.500, 0.000) - A(-0.500, 0.500, 0.000) – B(-0.500, 0.000, 0.000) - D(-0.500, 0.000, 0.500) - E(-0.500, 0.500, 0.500) - C(0.000, 0.500, 0.500), as illustrated in Fig. S1. Calculations were conducted for a total of 12 ions in a monoclinic cell (space group $P2_1/c$), with optimized cell parameters determined.

2.4. Characterization methods

The iron-cobalt niobate samples were characterized by X-ray diffraction (XRD) using a PANalytical X-ray diffractometer equipped with a Cu X-ray tube ($K\alpha_1$ = 1.540598 Å). Data were collected in the range of 20–70° with a step size of 0.02° and a counting time of 2s per step. The lattice parameters of the crystal structures were refined using the Rietveld method implemented in GSAS II software. The vibrational properties of the samples were investigated using a Raman microspectrometer (Horiba LabRam HR Evolution), which is equipped with a Synapse CCD detector, a high-stability BXFM open-space confocal microscope, and a 600 g/mm grating, with 532 nm excitation. Raman spectra were recorded for the different samples over a wavenumber range of 100–900 cm^{-1}. Morphological analyses were performed using a high-resolution scanning electron microscope (SEM) Vega3 SBH model from TESCAN, equipped with an energy-dispersive spectrometer (EDS) (Bruker Xflash 410 M). The energy electron acceleration voltage was set to 20 kV.

3. Results and discussions

The XRD analysis of the synthesized polycrystalline $Fe_{(1-x)}Co_xNbO_4$ ($0.0 \leq x \leq 0.20$) samples was conducted to gain further insights into the crystal structure and phase composition. Fig. 1(a) shows the X-ray diffraction patterns, which revealed that the samples exhibit a monoclinic phase belonging to the space group $P2_1/c$ (C_{2h}^{13}) (13), indexed using the ICDD standard (00-070-2275). The XRD patterns display a peak at ~23.6°, corresponding to the (110) plane, characteristic of the monoclinic phase [16,17]. Minor impurities were also observed and identified as belonging to phases such as Fe_2O_3 (ICSD-082902) and $CoFe_2O_4$ (COD-1533162). However, the presence of spurious phases like iron oxide (Fe_2O_3) in iron niobate ($FeNbO_4$) samples is widely reported in the literature [16,20,40]. Fig. 1(b) illustrates the unit cell of the monoclinic $FeNbO_4$ phase with Co^{2+} ions substituting for Fe^{3+} ions. The Fe/Co and Nb atoms are coordinated by six oxygen atoms. Furthermore, the Fe/Co atoms form edge-sharing FeO_6/CoO_6 octahedra, creating zigzag chains parallel to the c-axis. These zigzag chains intersect with similar chains formed by edge-sharing NbO_6 octahedra, as depicted in Fig. 1(c) and (d).

Fig. 2(a)–(e) presents the observed, calculated, differential, and Bragg position patterns from XRD Rietveld refinements for the $Fe_{(1-x)}Co_xNbO_4$ ($0.0 \leq x \leq 0.20$) samples. The observed and calculated patterns are depicted as open circles and solid red lines, respectively. The

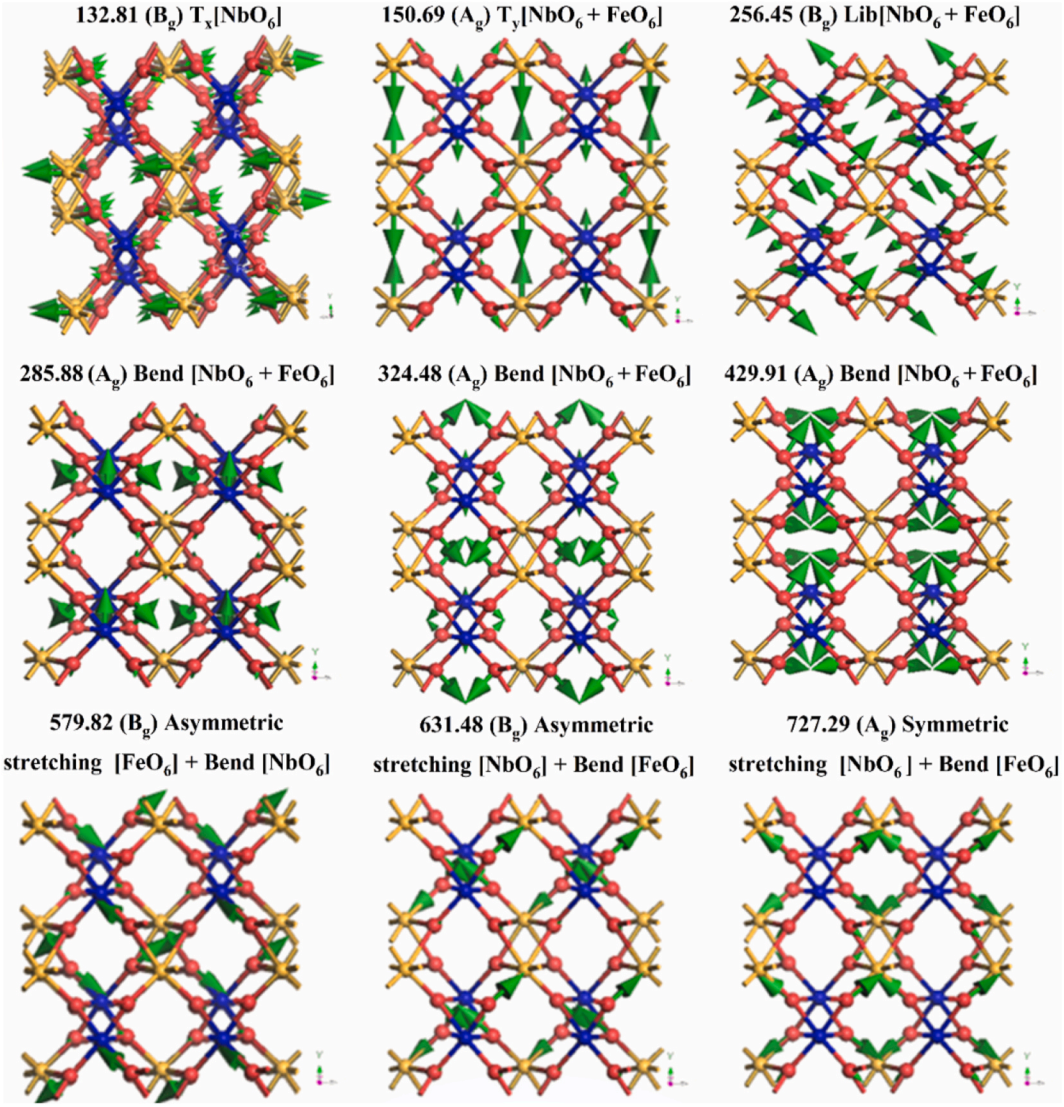

Fig. 4. Calculated wavenumbers and atomic displacements for some Raman modes of the iron niobate $FeNbO_4$.

refined parameters-lattice parameters, unit cell volume, occupancy, bond length, bond angle and atomic positions-are summarized on Tables S1 and S2. The fitting parameters, $R_{wp} = 16.33–17.79$ % and $\chi^2 = 1.32–1.69$, indicate a good agreement between the refined and observed XRD patterns for the monoclinic $FeNbO_4$ phase. Interestingly, a reduction in Nb–O bond lengths and an increase in almost all (Fe/Co)–O bond lengths were observed with increasing Co^{2+} content (summarized on Table S2). This result is attributed to the difference in ionic radii between Fe^{3+} (0.640 Å) and Co^{2+} (0.745 Å), which causes variations in bond lengths involving Fe/Co, also reported in the literature for Cu^{2+} [16]. Furthermore, Figs. S2(a)–(d) depicts the changes in lattice parameters and unit cell volume upon introduction of Co^{2+} ions into the $FeNbO_4$ structure. The lattice parameters exhibit an almost linear variation with the increase Co^{2+} content, ranging from $x = 0$ to 0.20. Similarly, changes in the unit cell volume correspond closely to those in the lattice parameters. The overall volume change was estimated to be $\Delta V/V = +1.14$ % as the cobalt doping increased to 0.20. The observed variations suggest an underlying anisotropy in the structure.

Vibrational Raman modes were determined by calculating the spatial derivatives of the macroscopic polarizations, as described by Porezag and Pederson [41]. These derivatives were computed numerically along the eigenvectors associated with each Raman-active phonon mode. By employing the linear response formalism, the polarization for each atomic displacement was calculated, facilitating the determination of the Raman susceptibility tensor. This tensor provides the fundamental basis for calculating the Raman intensity, as described in Equation (2).

$$A^m_{\alpha\beta} = \sqrt{V}\sum_{I\gamma}\frac{d\chi^{(1)}_{\alpha\beta}}{dR_{I\gamma}}\frac{\upsilon^m_{I\gamma}}{\sqrt{M_I}} \quad (2)$$

The first-order dielectric susceptibility, denoted as $\chi^{(1)}_{\alpha\beta}$, is influenced by the phonon eigenvector υ, which describes the direction of atomic displacement for atom I at its equilibrium position R when excited by a phonon mode m within a unit cell of volume V, as described in Ref. [42]. Raman mode assignments were performed via DFT calculation, yielding a satisfactory agreement with the experimental Raman spectra. The primitive cell, containing two formula units per unit cell, allows for a factor group analysis that predicts a total of 33 optical modes (at k = 0) and 3 acoustic modes for the $FeNbO_4$ crystal structure. The distribution of the optical modes according to the irreducible representations in the factor group C_{2h} is $8A_g + 10B_g + 6A_u + 6B_u$, with the acoustic modes being $A_u + 2B_u$. The selection rules only support A_g modes and B_g modes as Raman active. The Raman spectrum shown in Fig. 3 reveals 18 possible active vibrational modes, with at least 16 distinct bands identified in the experimental data. Raman wavenumbers in the spectral region of 100–900 cm^{-1} were calculated using the GGA-PBE functional.

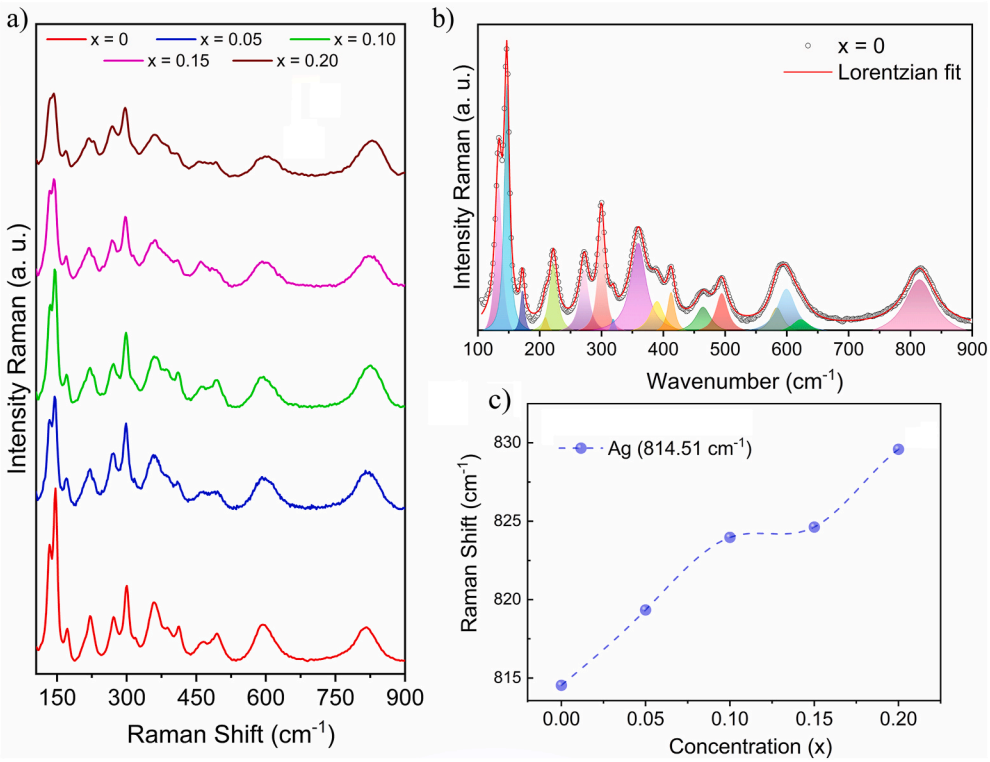

Fig. 5. (a) Spectra Raman of the $Fe_{(1-x)}Co_xNbO_4$ ($0 \leq x \leq 0.20$) samples; (b) deconvolution profile of the Raman modes for $x = 0$; and (c) displacement as a function of Co^{2+} concentration, showing the influence of Co^{2+} on the vibration modes 814.51 cm^{-1}.

The number of experimental modes is smaller than those predicted theoretically, which can be attributed to the following factors: i) some modes have closely spaced energies, making them challenging to resolve; (ii) weak bands may be obscured by more intense neighboring bands; and (iii) band resolution may be limited due to the random orientation of the crystals in the sample.

According to the DFT calculations, the vibrational modes involve significant contributions of the Fe–O and Nb–O bonds. The translational Raman modes of the polyhedral units located at 132.81 (B_g), 150.69 (A_g), 157.69 (B_g) and 233.02 (B_g) cm^{-1}, are assigned respectively as: T_x [NbO_6], T_Y [NbO_6 + FeO_6], T_{XZ} [NbO_6 + FeO_6] in the diagonal of the plane xz and T_{XYZ} [NbO_6+ FeO_6]. The librational modes appear located at 256.45 (B_g) Lib [NbO_6 + FeO_6] and 364.90 (B_g) cm^{-1} Lib [NbO_6 + FeO_6], while the bending modes of the [NbO_6 + FeO_6] units are: 285.88 (A_g), 324.48 (A_g), 339.11 (B_g), 364.90 (B_g), 429.91 (A_g), 440.50 (B_g), 462.05 (A_g), 470.31 (B_g) and 488.22 (A_g) cm^{-1}. The mode at 579.82 cm^{-1} (B_g) is assigned to a combination of an asymmetric stretching of [FeO_6] plus a bending of [NbO_6]. The mode at 631.48 cm^{-1} (B_g) is attributed to the asymmetric stretching of [NbO_6] combined with the bending of [FeO_6]. Finally, the modes at 588.14 (A_g) and 727.29 (A_g) cm^{-1} are assigned to the symmetric stretching of [NbO_6] plus a bending of [FeO_6]. Some important vibrations related to the motion of the Fe, O and Nb atoms are described in Table 1. Fig. 4 shows the calculated wavenumbers and atomic displacements for some Raman modes of $FeNbO_4$.

Fig. 5(a) presents the Raman spectra of $Fe_{(1-x)}Co_xNbO_4$ ($0 \leq x \leq 0.20$) samples, with the deconvolution of the bands shown specifically for the x = 0 sample in Fig. 5(b). The deconvoluted Raman bands for the remaining $Fe_{(1-x)}Co_xNbO_4$ ($0.05 \leq x \leq 0.20$) samples, are provided in Figs. S3(a)–(d). Table S3 shows the observed Raman shifts obtained from the deconvolution of the spectra of these samples. Fig. 5(c) highlights a significant shift in the Raman band observed in the undoped material at 814.51 cm^{-1}, assigned to a combination of the symmetric stretching of the [NbO_6] bonds with a [FeO_6] bending. This shift likely results from the incorporation of smaller ionic radius Co^{2+} ions into the A-site, consistent with findings reported in the literature [16,43]. Indeed, increasing the Co^{2+} amount in place of Fe^{3+} induces structural changes, including a reduction in Nb–O bond lengths and an increase in Fe/Co–O bond lengths (as shown in Table S2). This also results in the broadening of the Raman bands, which may be attributed to cationic disorder arising from the increase presence of Co^{2+}, as it is also corroborated by literature findings [44].

The morphology of $Fe_{(1-x)}Co_xNbO_4$ ($0.0 \leq x \leq 0.20$) samples were analyzed using scanning electron microscope (SEM). The SEM images in Fig. 6(a)–(e) reveal irregularly shaped particles with a range of sizes. Figs. S4(a)–(e) presents the particle size distributions for the sintered samples, showing an increase in grain size with Co doping, ranging from 5.07 ± 0.19 μm $\leq D \leq 13.60 \pm 0.33$ μm, with a mean grain size estimated of $\langle D \rangle = 9.04 \pm 0.25$ μm. The crystal structure of $FeNbO_4$ consists of FeO_6 and NbO_6 octahedra (Fig. 1), which contribute significant rigidity to the structure. However, when Fe^{3+} is partially substituted by Co^{2+}, defects are introduced, reducing the rigidity of the octahedra. This strain leads to modifications in bond angles and lengths. EDS spectra for $Fe_{(1-x)}Co_xNbO_4$ ($0.0 \leq x \leq 0.20$) samples are shown in Fig. S5, indicating the presence of Fe, Nb, and O ions for $x = 0$, with Co incorporation evident for $x = 0.05$–0.20. Table S1 shows that lattice parameters and unit cell volume increase with Co content, which correlates with the observed increase in grain size.

The electrocatalytic performance of $Fe_{(1-x)}Co_xNbO_4$ ($0.0 \leq x \leq 0.20$) iron niobate oxides for the HER was systematically evaluated across varying Co concentrations, as illustrated in Fig. 7. The electrocatalytic activity of the catalysts was initially assessed through linear sweep voltammetry (LSV) curves, shown in Fig. 7(a). In studies of new electrocatalytic materials for HER, the overpotential at a current density of 10 mA/cm^2, derived from LSV curves, is a key performance metric, as it represents the operating current density for water-splitting devices with efficiency of 12.3 % [45,46]. For $x = 0$, the catalyst exhibited lower HER activity, requiring an overpotential of 684 mV to achieve 10 mA/cm^2. In

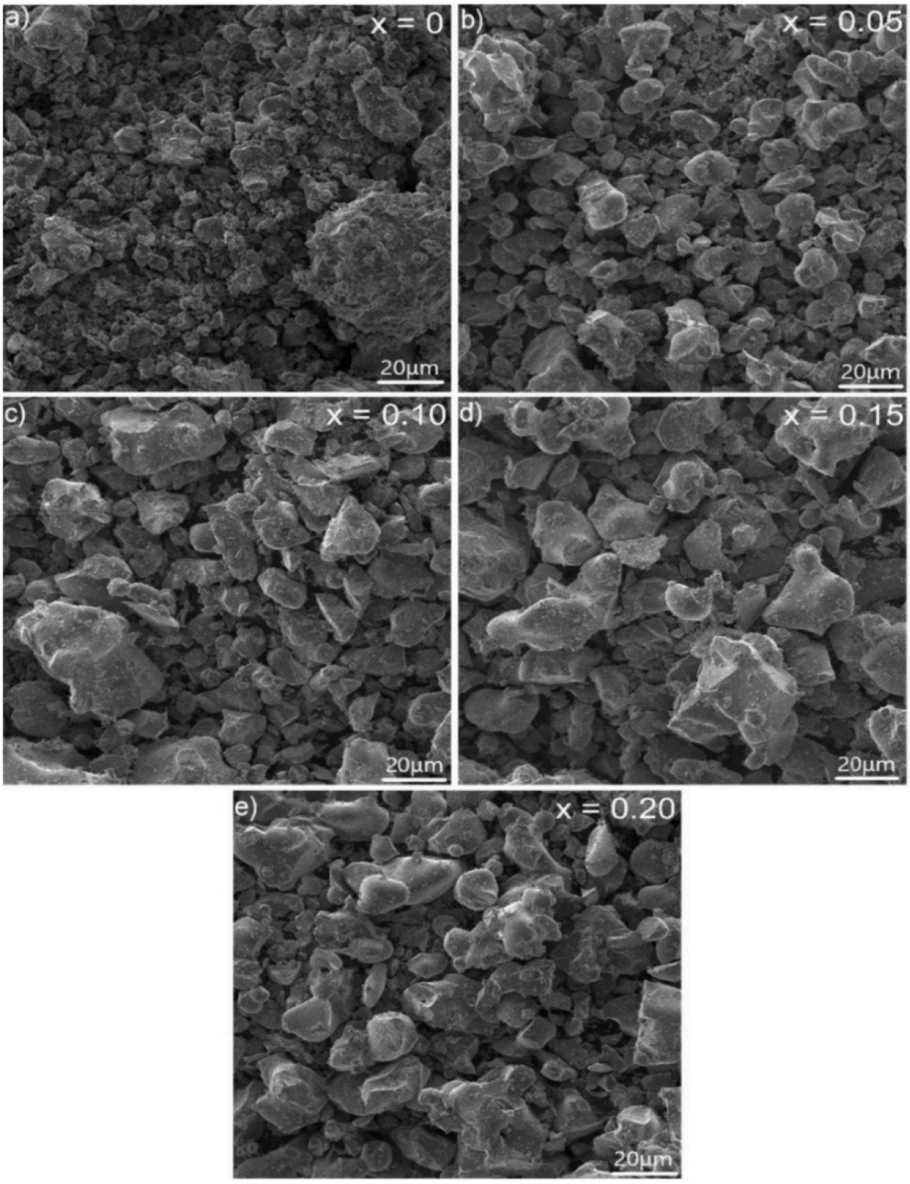

Fig. 6. SEM micrographs for $Fe_{(1-x)}Co_xNbO_4$ polycrystalline. (a) $x = 0.0$, (b) $x = 0.05$, (c) $x = 0.10$, (d) $x = 0.15$ and (e) $x = 0.20$.

contrast, with increasing Co^{2+} concentration, a reduction in the overpotential at 10 mA/cm^2 was observed, with values of 663 mV and 620 mV for $x = 0.10$ and $x = 0.20$, respectively. These findings indicate that Co^{2+} incorporation into $FeNbO_4$ iron niobate oxide significantly enhances the electrocatalytic properties of the material. However, previous studies have identified an optimal cobalt doping concentration, beyond which the further increases in concentration do not lead to improved catalytic performance. Wang et al. [47] demonstrated that excessive doping of FeS_2 with Co^{2+} (>10 %) can lead to the formation of undesirable phases, compromising charge transfer efficiency. Similarly, Wang et al. [48] investigated the doping of $FePS_3$ with Co^{2+} and found that cobalt addition enhances conductivity and HER kinetics up to an optimal point (>15 %), beyond which performance declines due to structural changes affecting the exposure of active sites and charge transfer efficiency, possibly as a result of structural effects that hinder the availability of active sites for hydrogen adsorption. The observed improvement in electrocatalytic activity is attributed to the low adsorption energy of H^+ protons at the Co^{2+} sites. Previous DFT studies by Fang Liu et al. [49], Guoqing Huang et al. [50], and Zhiming Liu et al. [51], suggest that hydrogen adsorption free energy on Co sites of the catalyst surface is relatively low, facilitating proton adsorption and decreasing overpotential in Co-doped $FeNbO_4$ electrocatalysts, which in turn accelerates hydrogen gas evolution. Furthermore, in comparison to other electrocatalysts synthesized through similar methodologies, $Fe_{(1-x)}Co_xNbO_4$ ($0.0 \leq x \leq 0.20$) displays competitive performance, as detailed in Table 2.

To elucidate the kinetic mechanism governing the HER in $FeNbO_4$ iron niobate oxides doped with Co^{2+}, Tafel plots (overpotential vs. log | current density|) were constructed based on LSV curves, as shown in Fig. 7(b). The linear regions of these plots were analyzed using the Tafel equation, $\eta = a + b \bullet log|J|$, where η is the overpotential, b represents the Tafel slope, J is the current density, and a is a constant [52,53]. The analysis revealed Tafel slopes of 197 mV/dec for $x = 0$, 175 mV/dec for $x = 0.10$ and 156 mV/dec for $x = 0.20$. The reduction in the Tafel slope observed for the $x = 0.20$ electrocatalyst suggests accelerated reaction kinetics, consistent with its enhanced electrocatalytic activity. These results are comparable to those reported in the literature for other electrocatalysts produced by similar methods, as summarized in Table 2. In alkaline media, electrolytes, the HER typically proceeds via either the Volmer-Tafel or Volmer-Heyrovsky mechanisms [52]. The

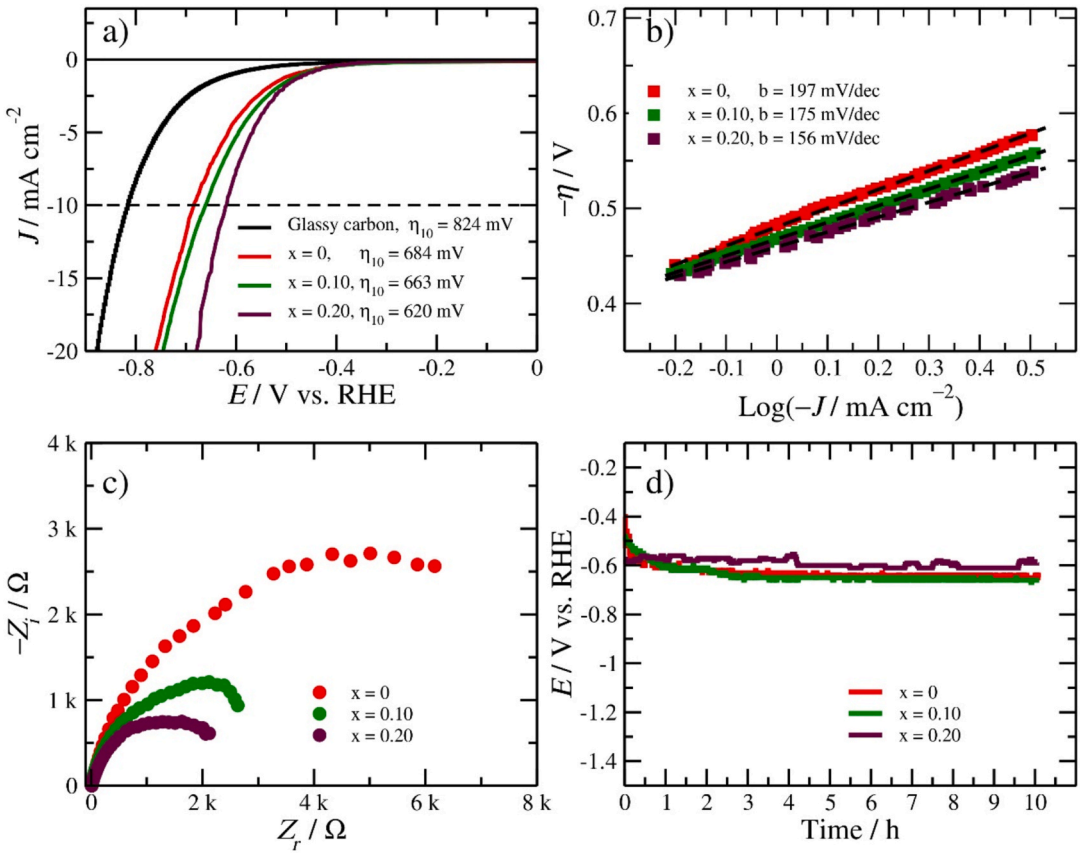

Fig. 7. Electrochemical test: (a) The polarization curves for HER electrocatalyst. (b) Tafel slope with linear fitting. (c) Nyquist plots from EIS. (d) Stability tests in continuous operation at 10 mA cm^{-2} for 10 h.

Table 2
Comparison electrocatalytic activity for HER of electrocatalyst $Fe_{(1-x)}Co_xNbO_4$ *with several recently reported electrocatalysts.*

Electrocatalysts	b/mV dec^{-1}	η/mV at 10 mA cm^{-2}	Reference
x = 0	***197***	***684***	***This work***
x = 0.10	***175***	***663***	***This work***
x = 0.20	***156***	***620***	***This work***
WO_3/NC	*137*	*745*	[55]
$SrLaFeO_4$	*258*	*691*	[56]
$SrLaCo_{0.5}Fe_{0.5}O_4$	*216*	*622*	[56]
MoS_2/C-600	*260*	*689*	[57]
Sr_3MnO_6	*240*	*590*	[58]
Fe–600C@BMC	*222*	*550*	[59]
Ni_3Fe@BC-600	*140*	*500*	[60]
Sr_3FeMnO_6	*214*	*450*	[58]
$SrNb_{0.1}Co_{0.7}Fe_{0.2}O_{3-\delta}$	*171*	*361*	[61]
$FeNbO_4$@C	*110*	*283*	[62]
$FeNbO_4$	*160*	*373*	[62]

rate-determining steps in these mechanisms, correspond to the Tafel, Heyrovsky and Volmer steps, associated with theoretical Tafel slopes of approximately 30, 40, and 120 mV/dec, respectively [52–54]. Given that the Tafel slopes observed for the studied catalysts exceed 120 mV/dec, the data suggest that the HER mechanism in these systems follows the Volmer–Heyrovsky pathway, with the Volmer step as the rate-limiting step.

The incorporation of Co^{2+} into electrocatalysts for HER, as demonstrated by Yu-Gang Fu et al. [63], plays a pivotal role in enhancing charge transfer during the reaction. This enhancement was systematically analyzed using EIS, with the corresponding Nyquist plots presented in Fig. 7(c). The data reveals a clear trend: increasing the Co^{2+} concentration in the electrocatalyst composition leads to a notable reduction in the arc circumference in the Nyquist plots. This decrease indicates lower charge transfer resistance, which directly correlates with an accelerated electron transfer rate, thereby significantly improving the catalytic efficiency of the material. These findings are consistent with the results obtained from the Tafel slope and overpotential analyses (Fig. 7(a) and (b)), which also demonstrate enhanced catalytic performance. Collectively, these results indicate that Co^{2+} not only reduces the energy barriers for charge transfer but also enhances the overall kinetics of the HER, making it a promising approach for improving electrocatalyst efficiency. Furthermore, the stability of the $x = 0$, $x = 0.10$, and $x = 0.20$ electrocatalysts was assessed through a constant electrolysis process, during which a current density of 10 mA/cm^2 was maintained for 10 h in a 1 mol/L NaOH solution, as shown in Fig. 6(d). The materials exhibited notable stability throughout the experiment, with the overpotential remaining relatively stable and showing minimal variation. The slight fluctuations in overpotential are likely due to the accumulation and release of H_2 bubbles on the catalyst surface [64]. These findings suggest that the materials demonstrate excellent stability and durability, crucial attributes for potential large-scale applications.

4. Conclusion

In conclusion, cobalt-doped $FeNbO_4$ were successfully synthesized via a solid-state reaction method. The resulting materials were subsequently evaluated for their potential as electrocatalysts in the HER. X-ray diffraction and Raman spectroscopy confirmed the formation of the $FeNbO_4$ phase with a monoclinic structure, space group $P2_1/c$ (C_{2h}^{13}). DFT calculations enabled the assignment of active Raman modes of the structure SEM and EDS analyses revealed irregularly shaped particles with increasing particle size as Co^{2+} concentration increased. Additionally, HER activity was assessed for samples with $x = 0$, $x = 0.10$, and

$x = 0.20$, highlighting enhancements in electrochemical performance with Co^{2+} incorporation. Electrochemical measurements demonstrated excellent stability and durability of the materials, which is attributed to efficient charge transfer, suggesting their potential for large-scale applications.

CRediT authorship contribution statement

Raí F. Jucá: Writing – original draft, Methodology, Investigation, Formal analysis, Data curation, Conceptualization. **Diego S. Evaristo:** Writing – original draft, Methodology, Investigation, Formal analysis, Conceptualization. **Francisco G.S. Oliveira:** Writing – review & editing, Writing – original draft, Methodology, Investigation, Data curation, Conceptualization. **Luís P.M. Santos:** Writing – original draft, Supervision, Investigation, Conceptualization. **Gilberto D. Saraiva:** Writing – review & editing, Writing – original draft, Validation, Supervision, Software, Resources, Project administration, Methodology, Investigation, Funding acquisition, Data curation, Conceptualization. **Antonio J. R. Castro:** Writing – review & editing, Supervision, Resources, Project administration, Investigation, Conceptualization. **Nilson S. Ferreira:** Writing – review & editing, Project administration, Methodology, Conceptualization. **Luiz F. Lobato:** Writing – original draft, Supervision, Software, Conceptualization. **João M. Soares:** Writing – original draft, Resources, Project administration, Methodology, Investigation, Conceptualization. **Anna Luiza B. Brito:** Writing – review & editing, Supervision, Resources, Conceptualization. **Rui Fausto:** Writing – original draft, Supervision, Resources, Project administration, Conceptualization. **Marcelo A. Macêdo:** Writing – review & editing, Supervision, Resources, Methodology, Conceptualization. **Benilde F.O. Costa:** Writing – review & editing, Supervision, Resources, Project administration, Conceptualization.

Declaration of competing interest

The authors declare that they have no known competing financial interests or personal relationships that could have appeared to influence the work reported in this paper.

Acknowledgements

G.D. Saraiva, Ph.D., acknowledges the support from the FUNCAP/Edital July 2021 (Grants# PS1-0186-00346.01.00/21), FUNCAP/Edital June 2023 (Grants# UNI-0210-00410.01.00/23), FUNCAP/Edital September 2023 (Grants# FPD-0213-00204.01.00/23) and the MCTI/CNPQ PQ – (Grants# 308449/2023-1). F. G. S. Oliveira D. da S. Evaristo thanks FUNCAP. L. P. M. Santos acknowledges CAPES and Federal University of Ceará for his visiting professor position (Grant number: 23067.054243/2023–93). A. J. R. Castro acknowledges the support from the MCTI/CNPQ PQ-09/2022 (Grants# 310440/2022-0). The authors would like to thank the Laboratório de Pesquisa em Corrosão (LPC) at the Federal University of Ceará for the infrastructure provided, which was essential for the completion of this study. This work was also supported by FCT - Fundação para a Ciência e Tecnologia, I.P. through the projects UIDB/04564/2020 and UIDP/04564/2020, with DOI identifiers 10.54499/UIDB/04564/2020 and 10.54499/UIDP/04564/2020, respectively. The support from the CAPES (PDSE Edital 2023/2024 - 88881.934165/2024-01) Access to TAIL-UC facility funded under QREN-Mais Centro Project No. ICT_2009_02_012_1890 is gratefully acknowledged. This work was also partially supported by Project PTDC/QUI-QFI/1880/2020, funded by Portuguese National Funds via FCT. The CQC-IMS is supported by FCT through projects UIDB/00313/2020 and UIDP/00313/2020 co-funded by COMPETE and the IMS special complementary funds provided by FCT. R.F thanks the European Research Agency and the Istanbul Kultur University (Istanbul, Türkiye) for the funding awarded to the ERA-Chair Spectroscopy@IKU project, and to Coimbra LaserLab for experimental Raman facilities.

Appendix A. Supplementary data

Supplementary data to this article can be found online at https://doi.org/10.1016/j.jpcs.2025.112649.

Data availability

Data will be made available on request.

References

[1] C.J. Winter, Into the hydrogen energy economy - milestones, Int. J. Hydrogen Energy 30 (2005) 681–685, https://doi.org/10.1016/j.ijhydene.2004.12.011.
[2] A. Midilli, M. Ay, I. Dincer, M.A. Rosen, On hydrogen and hydrogen energy strategies I : current status and needs, Renew. Sustain. Energy Rev. 9 (2005) 255–271, https://doi.org/10.1016/j.rser.2004.05.003.
[3] V.A. Goltsov, T.N. Veziroglu, From hydrogen economy to hydrogen civilization, Int. J. Hydrogen Energy 26 (2001) 909–915, https://doi.org/10.1016/S0360-3199(01)00045-3.
[4] M. Hirscher, Handbook of hydrogen storage. https://doi.org/10.1002/9783527629800, 2010.
[5] J. Greeley, T.F. Jaramillo, J. Bonde, I. Chorkendorff, J.K. Nørskov, Computational high-throughput screening of electrocatalytic materials for hydrogen evolution, Nat. Mater. 5 (2006) 909–913, https://doi.org/10.1038/nmat1752.
[6] W. Feng, W. Pang, Y. Xu, A. Guo, X. Gao, X. Qiu, W. Chen, Transition metal selenides for electrocatalytic hydrogen evolution reaction, Chemelectrochem 7 (2020) 31–54, https://doi.org/10.1002/celc.201901623.
[7] J. Zhang, Y. Liu, C. Sun, P. Xi, S. Peng, D. Gao, D. Xue, Accelerated hydrogen evolution reaction in CoS2 by transition-metal doping, ACS Energy Lett. 3 (2018) 779–786, https://doi.org/10.1021/acsenergylett.8b00066.
[8] Y. Abghoui, E. Skúlason, Hydrogen evolution reaction catalyzed by transition-metal nitrides, J. Phys. Chem. C 121 (2017) 24036–24045, https://doi.org/10.1021/acs.jpcc.7b06811.
[9] H. Du, R.M. Kong, X. Guo, F. Qu, J. Li, Recent progress in transition metal phosphides with enhanced electrocatalysis for hydrogen evolution, Nanoscale 10 (2018) 21617–21624, https://doi.org/10.1039/c8nr07891b.
[10] J. Wang, J. Liu, B. Zhang, X. Ji, K. Xu, C. Chen, L. Miao, J. Jiang, The mechanism of hydrogen adsorption on transition metal dichalcogenides as hydrogen evolution reaction catalyst, Phys. Chem. Chem. Phys. 19 (2017) 10125–10132, https://doi.org/10.1039/c7cp00636e.
[11] H. Jin, X. Liu, S. Chen, A. Vasileff, L. Li, Y. Jiao, L. Song, Y. Zheng, S.Z. Qiao, Heteroatom-doped transition metal electrocatalysts for hydrogen evolution reaction, ACS Energy Lett. 4 (2019) 805–810, https://doi.org/10.1021/acsenergylett.9b00348.
[12] Z. Liu, B. Tang, X. Gu, H. Liu, L. Feng, Selective structure transformation for NiFe/NiFe2O4 embedded porous nitrogen-doped carbon nanosphere with improved oxygen evolution reaction activity, Chem. Eng. J. 395 (2020) 125170, https://doi.org/10.1016/j.cej.2020.125170.
[13] A. Li, L. Zhang, F. Wang, L. Zhang, L. Li, H. Chen, Z. Wei, Rational design of porous Ni-Co-Fe ternary metal phosphides nanobricks as bifunctional electrocatalysts for efficient overall water splitting, Appl. Catal. B Environ. 310 (2022), https://doi.org/10.1016/j.apcatb.2022.121353.
[14] Y. Lian, Z. Xu, D. Wang, Y. Bai, C. Ban, J. Zhao, H. Zhang, Nb2O5 quantum dots coated with biomass carbon for ultra-stable lithium-ion supercapacitors, J. Alloys Compd. 850 (2021) 156808, https://doi.org/10.1016/j.jallcom.2020.156808.
[15] Y. Lian, D. Wang, S. Hou, C. Ban, J. Zhao, H. Zhang, Construction of T-Nb2O5 nanoparticles on/in N-doped carbon hollow tubes for Li-ion hybrid supercapacitors, Electrochim. Acta 330 (2020) 135204, https://doi.org/10.1016/j.electacta.2019.135204.
[16] D.S. Evaristo, R.F. Jucá, J.M. Soares, R.B. Silva, G.D. Saraiva, R.S. Matos, N. S. Ferreira, M. Salerno, M.A. Macêdo, Antiferromagnet–ferromagnet transition in Fe1−xCuxNbO4, Materials 15 (2022) 7424, https://doi.org/10.3390/ma15217424.
[17] N. Lakshminarasimhan, A.K.N. Kumar, S.S. Chandrasekaran, P. Murugan, Structure-magnetic property relations in FeNbO 4 polymorphs: a spin glass perspective, Prog. Solid State Chem. 54 (2019) 20–30, https://doi.org/10.1016/j.progsolidstchem.2019.03.001.
[18] C.B. Liu, R. Chen, X.Y. Yue, Y.J. Liu, M.M. Shi, H.P. Zhu, C. Dong, Y. Liu, Y.B. Han, J.F. Wang, Z.Z. He, Crystal growth, magnetic property and phase transition of the zigzag-chain antiferromagnet FeNbO4, J. Magn. Magn Mater. 464 (2018) 108–111, https://doi.org/10.1016/j.jmmm.2018.05.055.
[19] P. Moradi, E. Taheri-Nassaj, A. Yourdkhani, V. Mykhailovych, A. Diaconu, A. Rotaru, Dielectric, pyroelectric, and ferroelectric studies in (1 −x)AgNbO3-xFeNbO4 lead-free ceramics, Dalt. Trans. 52 (2023) 17894–17910, https://doi.org/10.1039/d3dt02864j.
[20] S. Devesa, F. Gonçalves, M. Graça, Influence of the preparation method on the structural, morphological and dielectric properties of FeNbO4 ceramics, Materials 16 (2023), https://doi.org/10.3390/ma16083202.
[21] A. Sreekumar, L. Durai, S. Badhulika, Solid-state single-step synthesis of FeNbO4 perovskite modified nickel foam for electrochemical detection of Creatine phosphokinase in simulated human blood serum, Ceram. Int. 49 (2023) 21722–21728, https://doi.org/10.1016/j.ceramint.2023.03.312.

[22] X. Wang, D. Santos-Carballal, N.H. de Leeuw, Oxygen diffusion in the orthorhombic FeNbO4 material: a computational study, Phys. Chem. Chem. Phys. 25 (2023) 6797–6807, https://doi.org/10.1039/d2cp04126j.
[23] X. Wang, D. Santos-Carballal, N.H. de Leeuw, Density functional theory study of monoclinic FeNbO4: bulk properties and water dissociation at the (010), (011), (110), and (111) surfaces, J. Phys. Chem. C 125 (2021) 27566–27577, https://doi.org/10.1021/acs.jpcc.1c05452.
[24] H. Fu, Y. Bai, Y. Lian, Y. Hu, J. Zhao, H. Zhang, Oxygen-deficient FeNbO 4-x in-situ growth in honey-derived N-doping porous carbon for overall water splitting, ChemSusChem 17 (2024) 1–10, https://doi.org/10.1002/cssc.202400162.
[25] Y. Cheng, S. Jabeen, S. Lei, N. Liu, Y. Liu, Y. Li, X. Wu, Z. Tong, J. Yu, P. Cao, Z. Kang, H. Li, N-doped carbon dots-modulated interfacial charge transfer and surface structure in FeNbO4 photocatalysts for enhanced CO2 conversion selectivity to CH4, Chem. Eng. J. 498 (2024) 155576, https://doi.org/10.1016/j.cej.2024.155576.
[26] S. Devesa, P.S.P. da Silva, M.P. Graça, M. Valente, L.C. Costa, J.A. Paixão, Electrical and magnetic characterization of Bi1 − xFexNbO4 ceramics, Ionics 27 (2021) 5347–5357, https://doi.org/10.1007/s11581-021-04263-y.
[27] H. Dong, T. Yao, X. Ji, Q. Zhang, X. Lin, B. Zhang, C. Ma, L. Meng, Y. Chen, H. Wang, Enhancing the lithium storage performance of the Nb2O5 anode via synergistic engineering of phase and Cu doping, ACS Appl. Mater. Interfaces 16 (2024) 22055–22065, https://doi.org/10.1021/acsami.4c03044.
[28] T.H. Jeon, A.D. Bokare, D.S. Han, A. Abdel-Wahab, H. Park, W. Choi, Dual modification of hematite photoanode by Sn-doping and Nb2O5 layer for water oxidation, Appl. Catal. B Environ. 201 (2017) 591–599, https://doi.org/10.1016/j.apcatb.2016.08.059.
[29] T. Takashima, H. Fukasawa, T. Mochida, H. Irie, Cu-doped Fe2O3 nanorods for enhanced electrocatalytic nitrogen fixation to ammonia, ACS Appl. Nano Mater. 6 (2023) 23381–23389, https://doi.org/10.1021/acsanm.3c04712.
[30] A. Samanta, S. Das, S. Jana, Doping of Ni in α-Fe2O3 nanoclews to boost oxygen evolution electrocatalysis, ACS Sustain. Chem. Eng. 7 (2019) 12117–12124, https://doi.org/10.1021/acssuschemeng.9b01208.
[31] Y.H. Wu, W.R. Guo, M. Mishra, Y.C. Huang, J.K. Chang, T.C. Lee, Combinatorial studies on wet-chemical synthesized Ti-doped α-Fe2O3: how does Ti4+ improve photoelectrochemical activity? ACS Appl. Nano Mater. 1 (2018) 3145–3154, https://doi.org/10.1021/acsanm.8b00316.
[32] Q. Zhu, M. Shao, S.H. Yu, X. Wang, Z. Tang, B. Chen, H. Cheng, Z. Lu, D. Chua, H. Pan, One-pot synthesis of Co-doped VSe2 nanosheets for enhanced hydrogen evolution reaction, ACS Appl. Energy Mater. 2 (2019) 644–653, https://doi.org/10.1021/acsaem.8b01659.
[33] H. Lin, N. Liu, Z. Shi, Y. Guo, Y. Tang, Q. Gao, Cobalt-doping in molybdenum-carbide nanowires toward efficient electrocatalytic hydrogen evolution, Adv. Funct. Mater. 26 (2016) 5590–5598, https://doi.org/10.1002/adfm.201600915.
[34] X. Dai, K. Du, Z. Li, M. Liu, Y. Ma, H. Sun, X. Zhang, Y. Yang, Co-doped MoS2 nanosheets with the dominant CoMoS phase coated on carbon as an excellent electrocatalyst for hydrogen evolution, ACS Appl. Mater. Interfaces 7 (2015) 27242–27253, https://doi.org/10.1021/acsami.5b08420.
[35] S.J. Clark, M.D. Segall, C.J. Pickard, P.J. Hasnip, M.I.J. Probert, K. Refson, M. C. Payne, First principles methods using CASTEP, Zeitschrift Fur Krist 220 (2005) 567–570, https://doi.org/10.1524/zkri.220.5.567.65075.
[36] D.R. Hamann, M. Schlüter, C. Chiang, Norm-conserving pseudopotentials, Phys. Rev. Lett. 43 (1979) 1494–1497, https://doi.org/10.1103/PhysRevLett.43.1494.
[37] J.P. Perdew, K. Burke, M. Ernzerhof, Generalized gradient approximation made simple, Phys. Rev. Lett. 77 (1996) 3865–3868, https://doi.org/10.1103/PhysRevLett.77.3865.
[38] J.D. Pack, H.J. Monkhorst, "special points for Brillouin-zone integrations"-a reply, Phys. Rev. B 16 (1977) 1748–1749, https://doi.org/10.1103/PhysRevB.16.1748.
[39] B.G. Pfrommer, M. Côté, S.G. Louie, M.L. Cohen, Relaxation of crystals with the quasi-Newton method, J. Comput. Phys. 131 (1997) 233–240, https://doi.org/10.1006/jcph.1996.5612.
[40] C. Iwasaki, Y. Yoshiyama, S. Hosokawa, N. Nagata, A. Dejima, K. Onishi, R. Maeda, S. Naniwa, S. Iguchi, H. Asakura, K. Teramura, T. Tanaka, Oxygen storage property and catalytic performance of Ti-doped FeNbO4, J. Phys. Chem. C 128 (2024) 9884–9893, https://doi.org/10.1021/acs.jpcc.4c01165.
[41] D. Porezag, M.R. Pederson, Infrared intensities and Raman-scattering activities within density-functional theory, Phys. Rev. B - Condens. Matter Mater. Phys. 54 (1996) 7830–7836, https://doi.org/10.1103/PhysRevB.54.7830.
[42] K. Miwa, Prediction of Raman spectra with ultrasoft pseudopotentials, Phys. Rev. B - Condens. Matter Mater. Phys. 84 (2011) 1–13, https://doi.org/10.1103/PhysRevB.84.094304.
[43] I.S. Cho, S. Lee, J. Hong-Noh, G.K. Choi, H.S. Jung, D.W. Kim, K.S. Hong, Visible-light-induced photocatalytic activity in FeNbO4 nanoparticles, J. Phys. Chem. C 112 (2008) 18393–18398, https://doi.org/10.1021/jp807006g.
[44] Q. Zhang, L. Xu, X. Tang, F. Huang, X. Wu, Y. Li, Y. Jing, Z.K. Han, H. Su, Electronic structure, Raman spectra, and microwave dielectric properties of Co-substituted ZnWO4 ceramics, J. Alloys Compd. 874 (2021) 159928, https://doi.org/10.1016/j.jallcom.2021.159928.
[45] N.T. Suen, S.F. Hung, Q. Quan, N. Zhang, Y.J. Xu, H.M. Chen, Electrocatalysis for the oxygen evolution reaction: recent development and future perspectives, Chem. Soc. Rev. 46 (2017) 337–365, https://doi.org/10.1039/c6cs00328a.
[46] J. Zhu, L. Hu, P. Zhao, L.Y.S. Lee, K.Y. Wong, Recent advances in electrocatalytic hydrogen evolution using nanoparticles, Chem. Rev. 120 (2020) 851–918, https://doi.org/10.1021/acs.chemrev.9b00248.
[47] D.-Y. Wang, M. Gong, H.-L. Chou, C.-J. Pan, H.-A. Chen, Y. Wu, M.-C. Lin, M. Guan, J. Yang, C.-W. Chen, Y.-L. Wang, B.-J. Hwang, C.-C. Chen, H. Dai, Highly active and stable hybrid catalyst of cobalt-doped FeS 2 nanosheets–carbon nanotubes for hydrogen evolution reaction, J. Am. Chem. Soc. 137 (2015) 1587–1592, https://doi.org/10.1021/ja511572q.
[48] S. Wang, B. Xiao, S. Shen, K. Song, Z. Lin, Z. Wang, Y. Chen, W. Zhong, Cobalt doping of FePS3promotes intrinsic active sites for the efficient hydrogen evolution reaction, Nanoscale 12 (2020) 14459–14464, https://doi.org/10.1039/d0nr03819a.
[49] F. Liu, W. He, Y. Li, F. Wang, J. Zhang, X. Xu, Y. Xue, C. Tang, H. Liu, J. Zhang, Activating sulfur sites of CoS2 electrocatalysts through tin doping for hydrogen evolution reaction, Appl. Surf. Sci. 546 (2021) 149101, https://doi.org/10.1016/j.apsusc.2021.149101.
[50] G. Huang, L. Zhao, S. Yuan, N. Li, S. Jing, Iron doped mesoporous cobalt phosphide with optimized electronic structure for enhanced hydrogen evolution, Int. J. Hydrogen Energy 47 (2022) 14767–14776, https://doi.org/10.1016/j.ijhydene.2022.02.223.
[51] Z. Liu, D. Gao, L. Hu, H. Liu, Y. Li, Y. Xue, F. Liu, J. Zhang, C. Tang, Boron-doped CoSe2 nanowires as high-efficient electrocatalyst for hydrogen evolution reaction, Colloids Surfaces A Physicochem. Eng. Asp. 646 (2022) 128903, https://doi.org/10.1016/j.colsurfa.2022.128903.
[52] J. Wang, F. Xu, H. Jin, Y. Chen, Y. Wang, Non-noble metal-based carbon composites in hydrogen evolution reaction: fundamentals to applications, Adv. Mater. 29 (2017), https://doi.org/10.1002/adma.201605838.
[53] J. Theerthagiri, S.J. Lee, A.P. Murthy, J. Madhavan, M.Y. Choi, Fundamental aspects and recent advances in transition metal nitrides as electrocatalysts for hydrogen evolution reaction: a review, Curr. Opin. Solid State Mater. Sci. 24 (2020) 100805, https://doi.org/10.1016/j.cossms.2020.100805.
[54] G. Zhao, K. Rui, S.X. Dou, W. Sun, Heterostructures for electrochemical hydrogen evolution reaction: a review, Adv. Funct. Mater. 28 (2018) 1–26, https://doi.org/10.1002/adfm.201803291.
[55] T. Feng, Z. Cui, P. Guo, X. Wang, J. Li, X. Liu, W. Wang, Z. Li, Fabrication of Ru/WO3-W2N/N-doped carbon sheets for hydrogen evolution reaction, J. Colloid Interface Sci. 636 (2023) 618–626, https://doi.org/10.1016/j.jcis.2023.01.054.
[56] M.S. Alom, F. Ramezanipour, Layered oxides SrLaFe1-xCoxO4-δ (x=0–1) as bifunctional electrocatalysts for water-splitting, ChemCatChem 13 (2021) 3510–3516, https://doi.org/10.1002/cctc.202100867.
[57] J.D. Yi, T.T. Liu, Y.B. Huang, R. Cao, Solid-state synthesis of MoS 2 nanorod from molybdenum-organic framework for efficient hydrogen evolution reaction, Sci. China Mater. 62 (2019) 965–972, https://doi.org/10.1007/s40843-018-9393-x.
[58] S.B. Karki, R.K. Hona, F. Ramezanipour, Sr3Mn2O6 and Sr3FeMnO6 for oxygen and hydrogen evolution electrocatalysis, J. Solid State Electrochem. 26 (2022) 1303–1311, https://doi.org/10.1007/s10008-022-05167-1.
[59] M.A. Ahsan, A.R. Puente Santiago, A. Rodriguez, V. Maturano-Rojas, B. Alvarado-Tenorio, R. Bernal, J.C. Noveron, Biomass-derived ultrathin carbon-shell coated iron nanoparticles as high-performance tri-functional HER, ORR and Fenton-like catalysts, J. Clean. Prod. 275 (2020) 124141, https://doi.org/10.1016/j.jclepro.2020.124141.
[60] Y.B. Adegbemiga, N. Ullah, M. Xie, S. Hussain, C.J. Oluigbo, W. Yaseen, A. J. Kumar, Y. Xu, J. Xie, Ni3Fe nanoparticles enclosed by B-doped carbon for efficient bifunctional performances of oxygen and hydrogen evolution reactions, J. Alloys Compd. 835 (2020) 155267, https://doi.org/10.1016/j.jallcom.2020.155267.
[61] Y. Zhu, W. Zhou, Y. Zhong, Y. Bu, X. Chen, Q. Zhong, M. Liu, Z. Shao, A perovskite nanorod as bifunctional electrocatalyst for overall water splitting, Adv. Energy Mater. 7 (2017) 10–17, https://doi.org/10.1002/aenm.201602122.
[62] H. Fu, Y. Bai, Y. Lian, Y. Hu, J. Zhao, H. Zhang, Oxygen-deficient FeNbO4-x in-situ growth in honey-derived N-doping porous carbon for overall water splitting, ChemSusChem 17 (2024) 1–10, https://doi.org/10.1002/cssc.202400162.
[63] Y.G. Fu, H.Q. Liu, C. Liu, Q.F. Lü, Ultralight porous carbon loaded Co-doped MoS2 as an efficient electrocatalyst for hydrogen evolution reaction in acidic and alkaline media, J. Alloys Compd. 967 (2023) 171748, https://doi.org/10.1016/j.jallcom.2023.171748.
[64] B.S. Singu, R.K. Chitumalla, D. Mandal, Y. Kim, G.H. Kim, H.T. Chung, J. Jang, H. Kim, Development of metal-organic framework-derived NiMo-MoO3−x porous nanorod for efficient electrocatalytic hydrogen evolution reactions, Appl. Catal. B Environ. 328 (2023) 122421, https://doi.org/10.1016/j.apcatb.2023.122421.